

Strongly Interacting Phases in Twisted Bilayer Graphene at the Magic Angle

Khagendra Adhikari¹, Kangjun Seo², K. S. D. Beach³ and Bruno Uchoa^{1*}

¹*Department of Physics and Astronomy, University of Oklahoma, Norman, OK 73069, USA*

²*School of Electrical and Computer Engineering,*

University of Oklahoma, Tulsa, OK 74135, USA and

³*Department of Physics and Astronomy, The University of Mississippi, University, MS 38677, USA*

(Dated: March 14, 2024)

Twisted bilayer graphene near the magic angle is known to have a cascade of insulating phases at integer filling factors of the low-energy bands. In this Letter we address the nature of these phases through an unrestricted, large-scale Hartree-Fock calculation on the lattice that self-consistently accounts for all electronic bands. Using numerically unbiased methods, we show that Coulomb interactions produce ferromagnetic insulating states at integer fillings $\nu \in [-3, 3]$ with maximal spin polarization $M_{\text{FM}} = 4 - |\nu|$. We find that the $\nu = 0$ state is a pure ferromagnet, whereas all other insulating states are spin-valley polarized. At odd filling factors $|\nu| = 1, 3$ those states have a quantum anomalous Hall effect with Chern number $\mathcal{C} = 1$. Except for the $\nu = 0, -2$ states, all other integer fillings have insulating phases with additional sublattice symmetry breaking and antiferromagnetism in the remote bands. We map the metal-insulator transitions of these phases as a function of the effective dielectric constant. Our results establish the importance of large-scale lattice calculations to faithfully determine the ground states of TBG at integer fillings.

Introduction.—When two graphene sheets are twisted by a small angle, dubbed the “magic angle,” their low energy bands reconstruct into flat bands [1, 2]. A cascade of insulating phases has been recently observed in twisted bilayer graphene (TBG) near the magic angle at integer filling fractions of the flat bands [3–7], some of which are in proximity to low-temperature superconducting phases [8–12]. Magic angle TBGs are considered strongly correlated electron systems, with evidence of a strange metal phase at finite temperature [13, 14] and of low-energy electronic collective modes that are strongly coupled to the charge carriers [15]. Because of the quantum geometry of the flat bands and the degeneracy between spin, valley, and sublattice degrees of freedom in graphene [16], interactions in combination with magnetic field, strain and substrate effects can drive various strongly interacting phases. Recent experiments observed evidence of quantum anomalous Hall (AQH) states [17–20], charge order [21], ferromagnetism [18], and Kekule intervalley coherent states [22–24] in the presence of strain.

The nature of intrinsic correlated insulating phases at zero field, in the absence of strain or substrate effects, is not clear. For instance, the insulating state at half-filling ($\nu = 0$) is unknown. Quantum Monte Carlo results in effective models predicted the possibility of valley quantum Hall [25, 26], intervalley coherent (IVC) states and a valence bond solid [25]. Hartree-Fock (HF) calculations found an antiferromagnet [27], a valley Chern insulator [28] and an IVC state [29]. Very little numerical results exist about the $|\nu| = 1$ states. A HF calculation found a Chern insulator with IVC states [23]. At $\nu = -2$, HF [27] and exact diagonalization [30] results encountered a pure spin polarized ferromagnet, whereas other HF results proposed a pure valley polarized state [31] and also an IVC state [23]. A growing consensus between HF and exact diagonalization at $|\nu| = 3$ indicates that

this state may be a spin-valley polarized Chern insulator [30, 32, 33]. The determination of these phases could shed light in the nature of the superconducting states in TBG and remains an outstanding open question.

At the magic angle $\theta \approx 1.1^\circ$, the Moiré unit cell with size $L \sim a/[2 \sin(\theta/2)] \approx 12$ nm, where a is the graphene lattice constant, has $\sim 10^4$ lattice sites, making *ab initio* methods prohibitively expensive. Previous numerical studies based on Hartree-Fock [28, 29, 31, 32, 34, 35], exact diagonalization [30, 33, 36], quantum Monte Carlo [25, 26], and density matrix renormalization group [37, 38] relied on effective low-energy models in the continuum approximation, or else in effective lattice models. The latter were derived either with the extraction of Wannier orbitals from the low-energy flat bands [39–44], phenomenologically [45], or else with the introduction of an energy cutoff in the remote bands [27].

Unlike in graphene monolayer, where continuum models are justified by the separation of the valleys through kinematic constraints [16], in TBG the valleys are not good quantum numbers even in the absence of backscattering [46, 47]. Besides, at length scales shorter than the size of the Moiré unit cell L , Coulomb interactions can be one order of magnitude larger than the energy gap separating the low-energy bands from the remote ones. A more conclusive determination of the ground state needs to account for virtual processes that connect the two sets of bands [48] and may require treating the remote bands on an equal footing with the flat ones through an unbiased calculation on the lattice.

In this Letter we perform an unrestricted, self-consistent, large-scale HF calculation on the lattice with Coulomb interactions screened only by metallic gates. The calculation fully accounts for all remote bands in the emergence of many-body states. We find that the insulating ground states of integer fillings $\nu \in [-3, 3]$ are

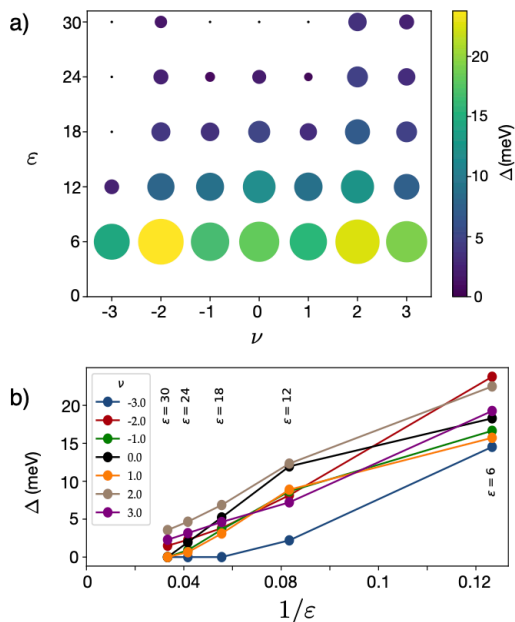


Figure 1: a) Phase diagram of strongly interacting phases in magic angle TBG at integer fillings $\nu \in [-3, 3]$ of the flat bands for different values of the effective dielectric constant ϵ . Size of the circles and color indicate the amplitude of the many-body gap Δ . Small dots are metallic states (zero gap), indicating the presence of a metal-insulator transition for a critical value of ϵ . b) Scaling of the many-body gap Δ vs $1/\epsilon$ for different integer fillings.

ferromagnetic, with a magnetic moment $M_{\text{FM}} = 4 - |\nu|$ due to the spin polarization of the flat bands. We find that the $\nu = 0$ state is a pure spin ferromagnet. Valley polarization (VP) is found at all integer ν away from $\nu = 0$. Except for $\nu = 0, -2$ we identified antiferromagnetism (AF) in the remote bands, which appears with sublattice polarization (SLP). Our results also indicate that odd filling factors $|\nu| = 1, 3$ have quantum anomalous Hall (QAH) states with Chern number $\mathcal{C}=1$, whereas even filling factors $|\nu| = 2$ have zero net Chern number. At $\nu < 0$ ($\nu > 0$), all flat bands with majority (minority) spin are topological, whereas the ones with minority (majority) spin are trivial. All bands are topologically trivial in the $\nu = 0$ state.

Those insulating states have a metal-insulator transition (MIT) at critical values of the effective dielectric constant ϵ , as shown in Fig. 1. The amplitudes of the many-body gaps for $|\nu| = 3$ are strongly particle-hole *asymmetric* in the moderate- and small-gap regimes, in agreement with experiments [5, 7] and in contrast with continuum models, which are particle-hole symmetric [49]. We conjecture that most experimental samples are in the vicinity of the $\nu = 0$ state MIT. In this regime, we find that the $\nu = \pm 2, 3$ states have prominent gaps of a few meV, whereas the other filling factors $\nu = -3, \pm 1$ are either metallic or have very small many-body gaps, also in

agreement with experiment. We suggest that these MIT transitions can be experimentally observed.

Hamiltonian.—We begin with the real space lattice Hamiltonian of TBG, $\mathcal{H} = \mathcal{H}_0 + \mathcal{H}_C$, where

$$\mathcal{H}_0 = \sum_{\alpha\beta} \sum_{ij} h_{\alpha\beta}(\mathbf{R}_i - \mathbf{R}_j) d_{\alpha,i,\sigma}^\dagger d_{\beta,j,\sigma} \quad (1)$$

is the hopping term, with $d_{\alpha,i,\sigma}$ the annihilation operator of an electron with spin $\sigma = \uparrow, \downarrow$ on sublattice α of unit cell i , and $h_{\alpha\beta}(\mathbf{R}_i - \mathbf{R}_j)$ is the corresponding tight-binding matrix element between sublattices α and β located in unit cells centered at \mathbf{R}_i and \mathbf{R}_j respectively. The second term describes a screened Coulomb interaction between any two lattice sites,

$$\mathcal{H}_C = \frac{1}{2} \sum_{\alpha\beta} \sum_{ij} \hat{n}_{\alpha,i} V_{\alpha\beta}(\mathbf{R}_i - \mathbf{R}_j) \hat{n}_{\beta,j}, \quad (2)$$

where $\hat{n}_{\alpha,i} = \sum_{\sigma} d_{\alpha,i,\sigma}^\dagger d_{\alpha,i,\sigma}$ is the local density operator and $V_{\alpha\beta}(\mathbf{R}) = e^2/(\epsilon\xi) \sum_{m=-\infty}^{\infty} (-1)^m [(|\boldsymbol{\tau}_\alpha - \boldsymbol{\tau}_\beta + \mathbf{R}|/\xi)^2 + m^2]^{-\frac{1}{2}}$ is the screened form of the interaction in the presence of symmetric gates located at the top and bottom of the TBG heterostructure [50, 51], with e the electron charge and $\boldsymbol{\tau}_\alpha$ the position of a site in sublattice α measured from the center of its unit cell. $\xi \approx 10$ nm is the distance between the plates of the metallic gates in most experiments [10, 12], and ϵ is the effective dielectric constant, which we treat as a free adjustable parameter. The value of the dielectric constant of graphene encapsulated in hexagonal boron nitride (hBN) is $\epsilon \approx 6$, although polarization effects due to remote bands in TBG could effectively make it several times larger [27, 30]. We regularize the on-site Coulomb interaction by choosing the onsite Hubbard term $V_{\alpha\alpha}(\mathbf{R} = 0) = 12.4/\epsilon$ eV of single layer graphene [52] and then smoothly interpolating it with Eq. (2) through $V_{\alpha\beta}(\mathbf{R}) \approx 1.438/[\epsilon(0.116 + |\boldsymbol{\tau}_\alpha - \boldsymbol{\tau}_\beta + \mathbf{R}|)]$ eV [53]. Although this choice is not unique, the results do not depend on the details of the regularization.

Strain effects can favor ground states that break the translational symmetry of the Moiré pattern [22–24]. To the best of our knowledge, no broken translation symmetry has been observed to date in TBG without strain [54, 55]. We assume the absence of strain effects and rewrite the Hamiltonian in momentum representation,

$$\mathcal{H} = \sum_{\alpha\beta} \sum_{\mathbf{k},\sigma} h_{\alpha\beta}(\mathbf{k}) d_{\alpha,\mathbf{k},\sigma}^\dagger d_{\beta,\mathbf{k},\sigma} + \mathcal{H}_C, \quad (3)$$

where

$$\mathcal{H}_C = \frac{1}{2} \sum_{\alpha\beta} \sum_{\mathbf{q}} \hat{n}_\alpha(\mathbf{q}) V_{\alpha\beta}(\mathbf{q}) \hat{n}_\beta(-\mathbf{q}), \quad (4)$$

with $V_{\alpha\beta}(\mathbf{q})$ being the Fourier transform of the Coulomb interaction in Eq. (2).

Near the magic angle $\theta \approx 1.085^\circ$ the unit cell of the commensurate structure has $N_b = 11164$ lattice sites,

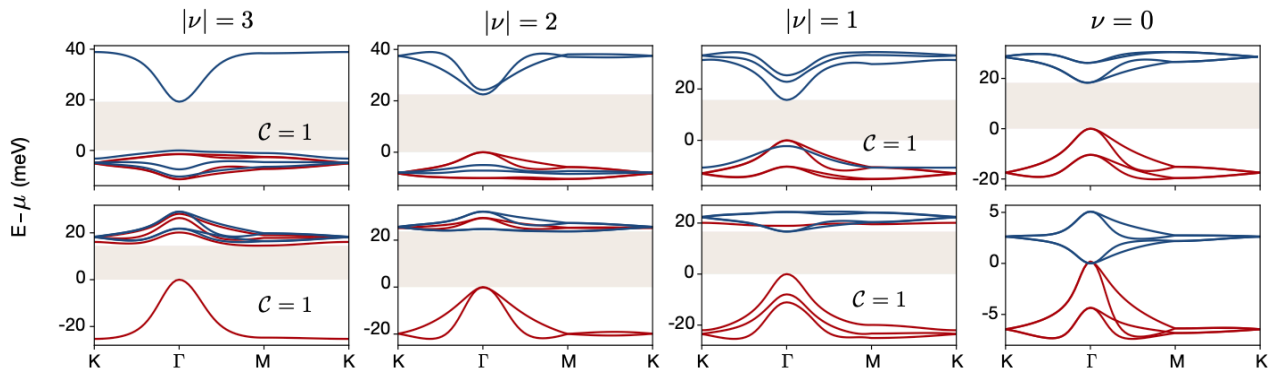


Figure 2: Band structure of the low energy spin polarized bands for integer filling factors. Top row from left to right: $\nu = 3, 2, 1, 0$ for $\varepsilon = 6$. Bottom row (left to right): $\nu = -3, -2, -1$ for $\varepsilon = 6$ and $\nu = 0$ for $\varepsilon = 30$ (metallic state). The gray shadow indicates the size of the many-body gap. Red (blue) lines represent spin σ ($-\sigma$). For $\nu < 0$ ($\nu > 0$) all red (blue) bands are topological, while blue (red) bands are trivial. Odd and even filling factors have a net Chern number $\mathcal{C} = 1$ and zero, respectively. At $\varepsilon = 6$ all integer filling factors have insulating states. The insulating state at $\nu = 0$ is ferromagnetic, with zero valley polarization. All non-zero filling states are spin and valley polarized. The $\nu = 0$ state has a MIT in the range $24 < \varepsilon < 30$ (see text).

and $\alpha = 1, \dots, N_b$. The tight-binding hopping parameters $t(\mathbf{r})$ are calculated from the standard Slater-Koster functions parametrized by *ab initio* calculations [56, 57]. We define $h_{\alpha\beta}(\mathbf{R}_i - \mathbf{R}_j) \equiv t(\mathbf{r}_\alpha - \mathbf{r}_\beta) - \mu\delta_{\alpha\beta}\delta_{ij}$, with $\mathbf{r}_\alpha = \tau_\alpha + \mathbf{R}_i$ the position of the lattice sites and μ the chemical potential. We account for lattice corrugation effects by allowing the layers to relax in the z direction. The relaxed tight-binding band structure of TBG has eight low energy bands with a band width of ~ 6 meV separated from the remote bands by an energy gap of 20 meV [40, 57–59]. At the Hartree level, charging effects are expected to significantly reconstruct the low energy bands [60].

Hartree-Fock calculation.—We proceed to identify the many-body ground states of the problem through an unrestricted, self-consistent HF calculation that accounts for *all* the electronic bands. A HF decomposition of the Hamiltonian reduces the problem to one of diagonalizing the effective Hamiltonian

$$\mathcal{H}_{\text{HF}} = \sum_{\mathbf{k}, \sigma} \sum_{\alpha\beta} \bar{h}_{\alpha\beta}(\mathbf{k}, \sigma) d_{\alpha, \mathbf{k}, \sigma}^\dagger d_{\beta, \mathbf{k}, \sigma}. \quad (5)$$

Here $\bar{h}_{\alpha\beta}(\mathbf{k}, \sigma) = h_{\alpha\beta}(\mathbf{k}) + h_{\alpha\beta}^{\text{H}}(\mathbf{k}, \sigma) + h_{\alpha\beta}^{\text{F}}(\mathbf{k}, \sigma)$ is the renormalized matrix elements due to both Hartree,

$$h_{\alpha\beta}^{\text{H}}(\mathbf{k}, \sigma) = \delta_{\alpha\beta} \sum_{\gamma, \mathbf{k}', \sigma'} V_{\beta\gamma}(0) \rho_{\gamma\gamma}(\mathbf{k}', \sigma'), \quad (6)$$

and Fock contributions,

$$h_{\alpha\beta}^{\text{F}}(\mathbf{k}, \sigma) = - \sum_{\mathbf{k}'} V_{\alpha\beta}(\mathbf{k} - \mathbf{k}') \rho_{\alpha\beta}(\mathbf{k}', \sigma). \quad (7)$$

Each contribution can be cast in terms of the $N_b \times N_b$ zero-temperature density matrix for a given momentum and spin,

$$\rho_{\alpha\beta}(\mathbf{k}, \sigma) = \sum_n^{\text{occupied}} \phi_{\alpha, \mathbf{k}}^{(n)}(\sigma) \phi_{\beta, \mathbf{k}}^{(n)*}(\sigma), \quad (8)$$

which is defined as a sum over all occupied bands, with $n = 1, \dots, N_b$. The N_b -component spinors $\phi_{\alpha, \mathbf{k}}^{(n)}(\sigma)$ describe the exact eigenvectors of Eq. (5), which need to be calculated self-consistently while enforcing a fixed total number of particles per unit cell.

The ground state at the HF level is found by self-consistently calculating the real space density matrix, $\hat{\rho}_{\alpha\beta}(\mathbf{R}, \sigma)$, from a 9×9 mesh in momentum space including the Γ point. Each self-consistent loop renormalizes the chemical potential of the previous step to ensure conservation of the total number of particles. All densities are measured away from the neutrality point. We subtract the density matrix from a reference density matrix corresponding to a uniform background of charge. The initial density matrix is extracted from the relaxed non-interacting tight binding Hamiltonian and self-consistently iterated until convergence. We implement a strong convergence criteria for the density matrix, where the root mean square of the difference in density matrices with the previous iteration is less than the tolerance, $\delta\hat{\rho}_{\alpha\beta}(0, \sigma) < 10^{-8}$. In order to probe for many-body instabilities, we seed the initial density matrix with random noise, allowing for all symmetries (with the exception of translational symmetry) to be broken. After convergence, we then perform numerical measurements with the resulting density matrix to identify the ground states at different filling factors. This approach provides an unbiased method to probe for many-body instabilities at the HF level.

Ferromagnetic ground states.—In Fig. 2 we show the reconstructed low energy bands of magic angle TBG for integer filling factors $\nu \in [-3, 3]$ for $\varepsilon = 6$. At this value of ε we find that all integer fillings correspond to insulating states. Interactions increase the bandwidth of the low-energy flat bands by a factor of ~ 3 , while splitting their spin degeneracy. The lines in red (blue) are

spin σ ($-\sigma$) bands, which are fully spin polarized, with large many-body gaps Δ (see Fig. 1a). For $\nu = -3$ the ground state is a ferromagnetic insulator with a single occupied flat band with spin σ , as depicted in Fig. 2. At higher non-positive integer fillings $\nu \leq 0$ the spin polarization M_{FM} increases in integer increments and is maximal at half filling ($\nu = 0$), where the ground state has four occupied mini-bands with the same spin σ . At positive integer fillings ($\nu > 0$) additional mini-bands with spin $-\sigma$ are occupied (see upper row of Fig. 2). We find that the system has maximum total spin polarization $M_{\text{FM}} = 4 - |\nu|$ for $\nu \in [-3, 3]$.

This behavior is observed in all insulating states at higher values of ε . For $\varepsilon = 12, 18, 24$ and 30 the many-body gaps progressively decrease while the low-energy bands become flatter, suggesting a series of filling-factor-dependent MITs [61]. For instance, at $\varepsilon = 18$ the $\nu = -3$ state is metallic whereas the $\nu = 0, \pm 1$ states have MITs in the range $24 < \varepsilon < 30$ (see Fig. 1). The $\nu = \pm 2, 3$ states are more robust, persisting at much larger values of ε . The scaling of Δ with $1/\varepsilon$ for all integer fillings is shown in Fig. 1b.

The ferromagnetic order parameter can be defined directly from the real-space density matrix as $M_{\text{FM}} = \sum_{\alpha} s_{\alpha}$, with $s_{\alpha} = \hat{\rho}_{\alpha\alpha}(0, \sigma) - \hat{\rho}_{\alpha\alpha}(0, -\sigma)$ the local spin polarization summed over all lattice sites in the Moiré unit cell. Only the flat bands contribute to the magnetization M_{FM} and to the ensuing ferromagnetic order. The ferromagnetic states are concentrated in AA site regions, where the charge density of the flat bands is also concentrated [62]. We summarize in Fig. 3a the explicit measurement of M_{FM} through the density matrix for different integer fillings.

With the exception of half and quarter filling ($\nu = 0, -2$), we find SLP in all other insulating states. The order parameter for SLP breaks the symmetry between sublattices A and B in each monolayer and is defined as $m_{\text{SLP}} = \sum_{\sigma, \alpha \in A} \hat{\rho}_{\alpha\alpha}(0, \sigma) - \sum_{\sigma, \alpha \in B} \hat{\rho}_{\alpha\alpha}(0, \sigma)$. In Fig. 3b we show the contribution to SLP from both the low-energy and remote bands. We find that SLP is accompanied by a sublattice modulation of the ferromagnetism in the low-energy bands, and by a pattern of *staggered* magnetization in the *remote* bands, indicating AF order [62]. In Fig. 3c we display the AF order parameter $M_{\text{AF}} = \sum_{\alpha \in A} s_{\alpha} - \sum_{\alpha \in B} s_{\alpha}$ for different integer fillings. Both M_{AF} and m_{SLP} vanish at $\nu = 0, -2$ and closely follow each other at other integer filling factors, as shown in Fig. 3b, c. We see weak SLP and AF order at $\nu = 2$.

Topological states.—We next calculate the Chern number of the flat bands through the eigenstates extracted from the self-consistent density matrix, $\mathcal{C}_n(\sigma) = -(i/2\pi) \int_{\text{BZ}} d^2k \hat{n} \cdot [\nabla_{\mathbf{k}} \times \langle \phi_{\mathbf{k}}^{(n)}(\sigma) | \nabla_{\mathbf{k}} | \phi_{\mathbf{k}}^{(n)}(\sigma) \rangle]$, with the integral set over the 2D Brillouin zone oriented in the \hat{n} -axis. In the panels of Fig. 2 we depict the Chern number of the topological flat bands with their corresponding spin polarization. At $\nu < 0$ all bands in red (spin σ) are

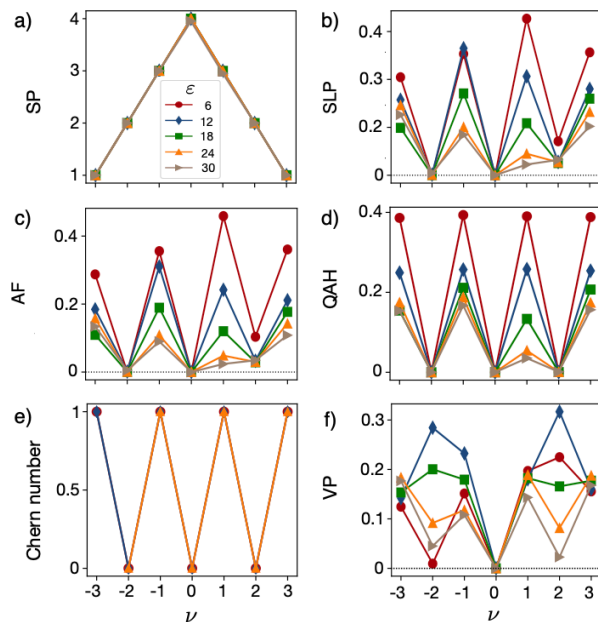


Figure 3: Magic angle TBG instabilities at $\varepsilon = 6$ (red dots), 12 (blue diamonds), 18 (green squares), 24 (orange triangles) and 30 (gray triangles) and for integer $\nu \in [-3, 3]$: a) Spin polarization, b) sublattice polarization, c) antiferromagnetism, d) quantum anomalous Hall, e) total Chern number and f) valley polarization. The $\nu = 0$ state has zero valley and sublattice polarization (see text).

topological, whereas the blue bands (spin $-\sigma$) are trivial. For $\nu > 0$ the blue bands become topological and the red ones trivial. All bands are trivial at $\nu = 0$. We find that the total Chern number of the occupied minibands with $|\nu| = 1, 3$ is $\mathcal{C} = 1$ for all values of ε with insulating states. At integer fillings $|\nu| = 0, 2$ the occupied mini-bands have zero net Chern number.

We verify this result by doing numerical measurements of the QAH order parameter through the real-space density matrix, $m_{\text{QAH}} = \frac{1}{3\sqrt{3}} \text{Im} \sum_{\langle\langle \alpha, \beta \rangle\rangle} \eta_{\alpha\beta} \hat{\rho}_{\alpha\beta}(0, \sigma)$, which probes for chiral loop currents among next-nearest-neighbor sites $\langle\langle \alpha, \beta \rangle\rangle$, where $\eta_{\alpha\beta} = \pm 1$ for clockwise or counterclockwise hopping in the honeycomb plaquette of each monolayer [63]. As shown in Fig. 3d, $m_{\text{QAH}} = 0$ at even filling factors and is finite at odd fillings, in agreement with the calculated Chern numbers depicted in Fig. 3e. We note that the $\nu = -3$ state for $\varepsilon \geq 18$ and $\nu = \pm 1$ for $\varepsilon = 30$ are spin polarized metals [61]. Although we observe bulk loop currents in this state ($m_{\text{QAH}} \neq 0$), they do not generate chiral topological edge modes and the Chern number is not well defined because of the finite Fermi surface around the Γ point.

Valley polarization.— In TBG the valleys are emergent quantum numbers that set the overall degeneracy of the flat bands in the non-interacting limit [64, 65]. To measure VP effects we use the order parameter $m_{\text{VP}} = \frac{1}{3\sqrt{3}} \text{Im} \sum_{\langle\langle \alpha, \beta \rangle\rangle} \delta_{\alpha} \eta_{\alpha\beta} \hat{\rho}_{\alpha\beta}(0, \sigma)$, with $\delta_{\alpha} = \pm 1$ for $\alpha \in A$

or B , which sums over the difference between the loop currents in sublattices A and B in each monolayer [47]. In Fig. 3f we show the total VP calculated for integer fillings. The behavior of m_{VP} is not monotonic with the strength of interactions. For all values of ε we find that VP and SLP are Pauli blocked at half filling, $m_{\text{VP}} = m_{\text{SLP}} = 0$, due to the $\nu = 0$ state being maximally spin polarized ($M_{\text{FM}} = 4$), exhausting the occupation of the flat bands with the same spin.

Discussion.—Exact diagonalization results [30] and exact calculations in the chiral limit of the continuum model [66] indicate that unrestricted HF may faithfully capture the ground state of magic angle TBG at integer fillings, where correlation effects are minimal, and interactions are mostly dominated by exchange. Transport experiments indicate the prevalence of insulating states at $\nu = \pm 2, 3$ [5, 7]. Our results, summarized in Fig. 1, correctly reproduce the observed hierarchy of many-body gaps separating those states from the $\nu = 0, \pm 1, -3$ ones for $\varepsilon \gtrsim 24$. Our results also correctly show a strong particle-hole asymmetry between the $\nu = \pm 3$ states, not captured in continuum models.

We note that our results at $\nu = 0$ strongly depart from prior quantum Monte Carlo and HF results in low energy effective models [25, 25–28], and indicate the presence of a pure spin ferromagnet with maximal polarization. The $\nu = \pm 1, \pm 3$ states are spin-valley polarized insulators with Chern number $\mathcal{C} = 1$, whereas the $\nu = \pm 2$ states are spin-valley polarized with zero net Chern number. The $\nu = \pm 2$ results depart from prior exact diagonalization and HF calculations in low energy models, which predicted either spin [27, 30] or valley polarized states [31]. On the other hand, our results at $\nu = \pm 3$ qualitatively agree with previous studies [30, 32, 33] and are consistent with zero-field transport measurements in hexagonal-boron nitride non-aligned samples [67]. We find that SLP is accompanied with the emergence of AF order in the remote bands at $\nu = \pm 3, \pm 1, 2$, and with sublattice modulation of the ferromagnetically ordered state in the flat bands. Recent electron spin resonance transport measurements have found evidence of magnetism and AF order in magic angle TBG at $\nu = \pm 2, 3$ [7].

Our numerical calculations also shed light into the MIT transition of those insulating states. The $\nu = 0$ insulator has been observed in some transport experiments [3] but not in others [5, 7]. According to the scaling of the many-body gaps shown in Fig. 1b, the typical transport gap for $\nu = -2$ is observed to be in the meV range in most HBN encapsulated samples, consistently with an effective dielectric constant $\varepsilon \sim 25 \pm 5$, close to the $\nu = 0$ state MIT. We predict that solid insulating behaviors at $\nu = 0$ and $\nu = \pm 1$ could be observed in suspended samples. Our results set the framework for the use of large-scale HF lattice calculations in moire heterostructures.

We acknowledge V. N. Kotov and E. Khalaf for helpful discussions. K. A. and B. U. acknowledge NSF grant

DMR-2024864 for support. We also acknowledge OSCER and MCSR supercomputing centers for support.

* Electronic address: uchoa@ou.edu

- [1] J. M. B. Lopes dos Santos, N. M. R. Peres, A. H. Castro Neto, Phys. Rev. Lett. **99**, 256802 (2007).
- [2] R. Bistritzer and A. H. MacDonald, Proc. Nat. Acad. Sci. U.S.A. **108**, 12233 (2011).
- [3] Y. Cao, V. Fatemi, A. Demir, S. Fang, S. L. Tomarken, J. Y. Luo, J. D. Sanchez-Yamagishi, K. Watanabe, T. Taniguchi, E. Kaxiras, R. C. Ashoori, and P. Jarillo-Herrero, Nature **582**, 80 (2018).
- [4] X. Lu, P. Stepanov, W. Yang, M. Xie, M. Ali Aamir, I. Das, C. Urgell, K. Watanabe, T. Taniguchi, G. Zhang, A. Bachtold, A. H. MacDonald, D. K. Efetov, Nature **574**, 653 (2019).
- [5] U. Zondiner, A. Rozen, D. Rodan-Legrain, Y. Cao, R. Queiroz, T. Taniguchi, K. Watanabe, Y. Oreg, F. von Oppen, Ady Stern, E. Berg, P. Jarillo-Herrero, and S. Ilani, Nature **582**, 203 (2020).
- [6] J. M. Park, Y. Cao, K. Watanabe, T. Taniguchi and Pablo Jarillo-Herrero, Nature **592**, 43(2021).
- [7] E. Morissette, J.-X. Lin, D. Sun, L. Zhang, S. Liu, D. Rhodes, K. Watanabe, T. Taniguchi, J. Hone, J. Pollanen, M. S. Scheurer, M. Lilly, A. Mounce, Nat. Phys. <https://doi.org/10.1038/s41567-023-02060-0> (2023).
- [8] Y. Cao, V. Fatemi, S. Fang, K. Watanabe, T. Taniguchi, E. Kaxiras, and P. Jarillo-Herrero, Nature **582**, 42 (2018).
- [9] M. Yankowitz, S. Chen, H. Polshyn, Y. Zhang, K. Watanabe, T. Taniguchi, D. Graf, A. F. Young, C. R. Dean, Science **363**, 1059 (2019).
- [10] P. Stepanov, I. Das, X. Lu, A. Fahimniya, K. Watanabe, T. Taniguchi, F. H. L. Koppens, J. Lischner, L. Levitov, D. K. Efetov, Nature **583** 375 (2020).
- [11] A. Jaoui, I. Das, Giorgio Di Battista Xiaobo Lu, K. Watanabe, T. Taniguchi, Jaime Díez-Mérida, H. Ishizuka, L. Levitov and D. K. Efetov, Nat. Physics **18**, 633 (2020).
- [12] Y. Saito, J. Ge, K. Watanabe, T. Taniguchi and A. F. Young, Nat. Phys. **16**, 926 (2020).
- [13] H. Polshyn, M. Yankowitz, S. Chen, Y. Zhang, K. Watanabe, T. Taniguchi, C. R. Dean and A. F. Young, Nat. Phys. **15**, 1011 (2019).
- [14] Y. Cao, D. Chowdhury, D. Rodan-Legrain, O. Rubies-Bigorda, K. Watanabe, T. Taniguchi, T. Senthil, and P. Jarillo-Herrero, Phys. Rev. Lett. **124**, 076801 (2020).
- [15] Y. Saito, F. Yang, J. Ge, X. Liu, T. Taniguchi, K. Watanabe, J. I. A. Li, E. Berg, and A. F. Young, Nature **592**, 220 (2021).
- [16] V. N. Kotov, B. Uchoa, V. M. Pereira, F. Guinea, and A. H. Castro Neto, Rev. Mod. Phys. **84**, 1067 (2012).
- [17] E. M. Spanton, A. A. Zibrov, H. Zhou, T. Taniguchi, K. Watanabe, M. P. Zaletel, and A. F. Young, Science **360**, 62 (2018).
- [18] A. L. Sharpe, E. J. Fox, A. W. Barnard, J. Finney, K. Watanabe, T. Taniguchi, M. A. Kastner, and D. Goldhaber-Gordon, Science **365**, 605 (2019).
- [19] M. Serlin, C. L. Tschirhart, H. Polshyn, Y. Zhang, J. Zhu, K. Watanabe, T. Taniguchi, L. Balents, and A. F.

- Young, *Science* **367**, 900 (2020).
- [20] S. Wu, Z. Zhang¹, K. Watanabe, T. Taniguchi and E. Y. Andrei, *Nat. Materials* **20**, 488 (2021).
- [21] Y. Jiang, X. Lai, K. Watanabe, T. Taniguchi, K. Haule, J. Mao, and Y. Andrei, *Nature* **573**, 91 (2019).
- [22] K. P. Nuckolls, R. L. Lee, M. Oh, D. Wong¹, T. Soejima, J. P. Hong, D. Călugăru, J. Herzog-Arbeitman, B. A. Bernevig¹, K. Waanabe, T. Taniguchi, N. Regnault, M. P. Zaletel, A. Yazdani, arXiv:2303.00024 (2023).
- [23] G. Wagner, Y. H. Kwan, N. Bultinck, S. H. Simon, and S. A. Parameswaran, *Phys. Rev. Lett.* **128**, 156401 (2022).
- [24] Y. H. Kwan, G. Wagner, T. Soejima, M. P. Zaletel, S. H. Simon, S. A. Parameswaran, and N. Bultinck, *Phys. Rev. X* **11**, 041063 (2021).
- [25] Y. D. Liao, J. Kang, C. N. Breið, X. Yan Xu, Han-Qing Wu, B. M. Andersen, R. M. Fernandes, and Zi Yang Meng, *Phys. Rev. X* **11**, 011014 (2021).
- [26] J. S. Hofmann, E. Khalaf, A. Vishwanath, E. Berg, and J. Y. Lee, *Phys. Rev. X* **12**, 011061 (2022).
- [27] J. Gonzalez and T. Stauber, *Phys. Rev. B* **104**, 115110 (2021).
- [28] S. Liu, E. Khalaf, J. Yeon Lee, and A. Vishwanath, *Phys. Rev. Rev.* **3**, 013033 (2021).
- [29] N. Bultinck, E. Khalaf, S. Liu, S. Chatterjee, A. Vishwanath, and M. P. Zaletel, *Phys. Rev. X* **10**, 031034 (2020).
- [30] P. Potasz, M. Xie and A. H. MacDonald, *Phys. Rev. Lett.* **127**, 147203 (2021).
- [31] M. Xie and A. H. MacDonald, *Phys. Rev. Lett.* **124**, 097601 (2020).
- [32] F. Xie, J. Kang, B. A. Bernevig, O. Vafek, and N. Regnault, *Phys. Rev. B* **107**, 075156 (2023).
- [33] F. Xie, A. Cowsik, Z.-D. Song, B. Lian, B. A. Bernevig, and N. Regnault, *Phys. Rev. B* **103**, 205416 (2021).
- [34] T. Cea and F. Guinea, *Phys. Rev. B* **102**, 045107 (2020).
- [35] J. Liu and X. Dai, *Phys. Rev. B* **103**, 035427 (2021).
- [36] C. Repellin, Z. Dong, Y.-H. Zhang, and T. Senthil, *Phys. Rev. Lett.* **124**, 187601 (2020).
- [37] T. Soejima, D. E. Parker, N. Bultinck, J. Hauschild, and M. P. Zaletel, *Phys. Rev. B* **102**, 205111 (2020).
- [38] J. Kang, and O. Vafek, *Phys. Rev. B* **102**, 035161 (2020).
- [39] J. Kang, and O. Vafek, *Phys. Rev. X* **8**, 031088 (2018).
- [40] M. Koshino, N. F. Q. Yuan, T. Koretsune, M. Ochi, K. Kuroki, and L. Fu, *Phys. Rev. X* **8**, 031087 (2018).
- [41] J. Kang, and O. Vafek, *Phys. Rev. Lett.* **122** 246401 (2019).
- [42] K. Seo, V. N. Kotov, and B. Uchoa, *Phys. Rev. Lett.* **122** 246402 (2019).
- [43] C. N. Breið and B. M. Andersen, *Phys. Rev. B* **107**, 165114 (2023).
- [44] B. Andrews and A. Soluyanov, *Phys. Rev. B* **101**, 235312 (2020).
- [45] A. Khalifa, G. Murthy, and R. K. Kaul, *Phys. Rev. B* **107**, 235137 (2023).
- [46] In TBG, different valleys are coupled by hopping between the monolayers. At the tight-binding level, each state in the moire BZ is a non-trivial momentum dependent mixture of the two valleys. See Ref. [47].
- [47] A. Ramires and J. L. Lado, *Phys. Rev. B* **99**, 245118 (2019).
- [48] Previous attempts to incorporate remote band effects were mostly based on self-energy corrections to the flat bands in the form of interaction assisted hopping terms. See Ref. [25, 30, 41, 60].
- [49] Particle-hole symmetry is defined as invariance under the transformation $\nu \rightarrow -\nu$. See Ref. [30].
- [50] R. E. Throckmorton and O. Vafek, *Phys. Rev. B* **86**, 115447 (2012).
- [51] B. A. Bernevig, Zhi-Da Song, Nicolas Regnault, and Biao Lian, *Phys. Rev. B* **103**, 205413 (2021).
- [52] T. O. Wehling, E. Sasioglu, C. Friedrich, A. I. Lichtenstein, M. I. Katsnelson, and S. Blugel, *Phys. Rev. Lett.* **106**, 236805 (2011).
- [53] L. Rademaker, D. A. Abanin, and P. Mellado, *Phys. Rev. B* **100**, 205114 (2019).
- [54] Y. Xie, B. Lian, B. Jäck, X. Liu, C.-L. Chiu, K. Watanabe, T. Taniguchi, B. Andrei Bernevig, and A. Yazdani, *Nature* **572**, 101 (2019).
- [55] A. Kerelsky, L. J. McGilly, D. M. Kennes, L. Xian, M. Yankowitz, S. Chen, K. Watanabe, T. Taniguchi, J. Hone, Cory Dean, A. Rubio, and A. N. Pasupathy, *Nature* **572**, 95 (2019).
- [56] We set $t(\mathbf{r}) = \cos^2 \theta_z V_\sigma(\mathbf{r}) + \sin^2 \theta_z V_\pi(\mathbf{r})$, where $\cos \theta_z = d/|\mathbf{r}|$, with d the vertical distance between sites. $V_\sigma(\mathbf{r}) = V_\sigma^0 \exp[-(|\mathbf{r}| - d_0)/\lambda]$ and $V_\pi(\mathbf{r}) = V_\pi^0 \exp[-(|\mathbf{r}| - a/\sqrt{3})/\lambda]$ are Slater-Koster functions, with $V_\sigma^0 = -0.48\text{eV}$, $V_\pi^0 = 0.27\text{eV}$, and $\lambda = 0.4525\text{\AA}$. $d_0 = 3.35\text{\AA}$ is the unrelaxed interlayer distance and $a = 2.42\text{\AA}$ the in-plane lattice constant. See Ref. [57].
- [57] N. N. T. Nam and M. Koshino, *Phys. Rev. B* **96**, 075311 (2017).
- [58] K. Uchida, S. Furuya, J.-I. Iwata, and A. Oshiyama, *Phys. Rev. B* **90**, 155451 (2014).
- [59] For details on the tight-binding band structure with lattice relaxation effects, see supplemental materials.
- [60] F. Guinea, and N. R. Walet, *Proc. Nat. Acad. Sci. U.S.A.* **115**, 131714 (2018).
- [61] For more details about the interacting band structure at different values of ε , see supplemental materials.
- [62] Details about the charge and spin distribution in the more unit cell are shown in the supplemental materials.
- [63] F. D. M. Haldane, *Phys. Rev. Lett.* **61**, 2015 (1988).
- [64] V. M. Pereira, V. N. Kotov, and A. H. Castro Neto, *Phys. Rev. B* **78**, 085101 (2008).
- [65] X. Dou, V. N. Kotov, B. Uchoa, *Sci. Rep.* **6**, 31737 (2016).
- [66] B. Lian, Z.-D. Song, N. Regnault, D. K. Efetov, A. Yazdani, and B. A. Bernevig, *Phys. Rev. B* **103**, 205414 (2021).
- [67] P. Stepanov, M. Xie, T. Taniguchi, K. Watanabe, X. Lu, A. H. MacDonald, B. Andrei Bernevig, and D. K. Efetov, *Phys. Rev. Lett.* **127**, 197701 (2021).

Supplementary Material of “Strongly Interacting Phases in Twisted Bilayer Graphene at the Magic Angle”

Khagendra Adhikari,^{1,*} Kangjun Seo,² K. S. D. Beach,³ and Bruno Uchoa^{1,†}

¹*Department of Physics and Astronomy, University of Oklahoma, Norman, Oklahoma 73019, USA*

²*School of Electrical and Computer Engineering,*

University of Oklahoma, Tulsa, Oklahoma 74135, USA

³*Department of Physics and Astronomy, The University of Mississippi, University, Mississippi 38677, USA*

(Dated: March 12, 2024)

TIGHT-BINDING CALCULATION

Twisted bilayer graphene

We rotate the top layer by $+\theta/2$ and the bottom layer by $-\theta/2$ about the z -axis passing through AA sites. For an arbitrary twist angle, commensuration between the layers requires that [1]

$$\cos(\theta^\circ) = \frac{3m^2 + 3ms + \frac{s^2}{2}}{3m^2 + 3ms + s^2}, \quad (1)$$

with m and s integers. The choice $s = 1$ and $m = 0$ corresponds to a 60° rotation (AA stacked untwisted bilayer), whereas $s = 1$, $m = 30$ corresponds to $\theta \approx 1.085$, which is close to the magic angle. The number of sites per unit cell is given by

$$N_b = 4(3m^2 + 3ms + s^2), \quad (2)$$

with the factor of 4 corresponding to the two sub-lattices in each layer and the two layers. The period of the moiré unit cell is $L = a/[2 \sin(\theta/2)]$, with $a = 2.46\text{\AA}$ the lattice constant corresponding to the carbon-carbon distance $a_0 = a/\sqrt{3}$.

In the rotated layers,

$$\mathbf{g}_i^{\text{bottom}} = R(-\theta/2)\mathbf{g}, \quad \mathbf{g}_i^{\text{top}} = R(\theta/2)\mathbf{g}, \quad R(\theta) = \begin{pmatrix} \cos \theta & \sin \theta \\ -\sin \theta & \cos \theta \end{pmatrix}, \quad (3)$$

where $\mathbf{g}_1 = 2\pi(1, -1/\sqrt{3})/a$ and $\mathbf{g}_2 = 2\pi(0, 2/\sqrt{3})/a$ are the original reciprocal lattice vectors of the monolayer.

Reciprocal space moiré superlattice vectors can be calculated as

$$\mathbf{G}_i = \mathbf{g}_i^{\text{bottom}} - \mathbf{g}_i^{\text{top}}, \quad i \in \{1, 2\}, \quad (4)$$

The corresponding real space moiré superlattice vectors are

$$\mathbf{T}_1 = m\mathbf{a}_1 + (m + s)\mathbf{a}_2, \quad \mathbf{T}_2 = R(\pi/3)\mathbf{T}_1, \quad (5)$$

with $\mathbf{a}_1 = a(1, 0)$ and $\mathbf{a}_2 = a(1/2, \sqrt{3}/2)$ the generators of the original Bravais lattice. The atomic positions in the monolayer unit cell are $\mathbf{r}_A = (0, 0)$ and $\mathbf{r}_B = (\mathbf{a}_1 + \mathbf{a}_2)/3 = a(1/2, 1/2\sqrt{3})$, whereas the coordinates of the hexagonal center are $\mathbf{r}_{HC} = (2\mathbf{a}_1 - \mathbf{a}_2)/3$.

To calculate tight-binding band structure we follow ref. 3 and adopt the Slater-Koster parametrization

$$t(\delta r) = V_\sigma \cos^2 \theta_z e^{-\frac{\delta r - d_0}{\lambda}} + V_\pi \sin^2 \theta_z e^{-\frac{\delta r - a_0}{\lambda}}, \quad (6)$$

where $\cos \theta_z = dz/\delta r$ with $\delta r = |\mathbf{r} - \mathbf{r}'|$ and $dz = |\mathbf{r}_z|$ [2]. $\lambda = 0.184a = 0.4525\text{\AA}$ is the p -orbital decay length, $V_\sigma = -0.48\text{eV}$ is the interlayer hopping when two carbon atoms are exactly above each other, $V_\pi = 2.7\text{eV}$ is the nearest-neighbors intralayer hopping strength, and $d_0 = 3.35\text{\AA}$ is the unrelaxed interlayer distance [3]. We implement the cutoff distance for hopping using a Heaviside step function $\Theta(5a_0 - r)$ including the first five nearest neighbor sites.

In the absence of corrugation the above parameters do not lead to a gap separating the flat bands from the remote ones (see Fig. 1). Corrugation due to lattice relaxation in the z direction increases (reduces) the interlayer distance

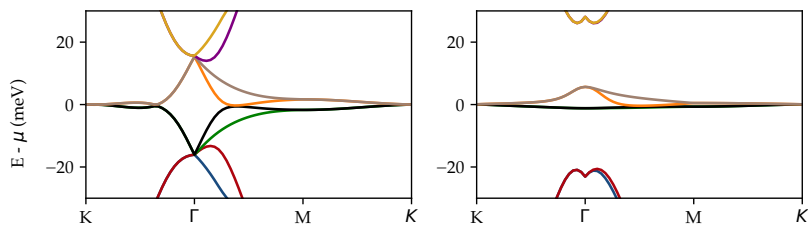


FIG. 1. Non-interacting tight-binding dispersion in the absence of lattice relaxation (left) and with relaxation (right), for optimized structure. Relaxation effects make the low energy bands flatter and stabilize a large gap of $\sim 20\text{meV}$ with the remote bands.

in $AA(AB)$ site regions [4]. The lattice relaxation in which the z -coordinate of the carbon atoms is parametrized as

$$\mathbf{r}_z(\mathbf{r}_{xy}) = d_0 + d_1 \sum_{i=1,2,3} \cos(\mathbf{G}_i \cdot \mathbf{r}_{xy}) \quad (7)$$

where $\mathbf{G}_i \in \{\mathbf{G}_1, \mathbf{G}_2, \mathbf{G}_3 = (\mathbf{G}_1 + \mathbf{G}_2)\}$ are shortest three reciprocal lattice vectors, $d_0 = (d_{AA}(\theta) + 2d_{AB})/3$, $d_1 = 2(d_{AA}(\theta) - d_{AB})/9$. The twist-angle dependent displacement can be written as [4]

$$d_{AA}(\theta) = d_{AB} + (d_{AA} - d_{AB}) \exp\{-0.009\theta^2\} \quad (8)$$

with $d_{AA} = 3.6\text{\AA}$ and $d_{AB} = 3.35\text{\AA}$ are the relaxed inter-layer distance at AA and AB regions, respectively [3, 4].

Coulomb Interaction

We consider Coulomb interactions screened by the metallic gates, consistently with the experimental setup. We use the following two-gated screened potential

$$U_1(\mathbf{r}) = U_\xi \sum_{m=-\infty}^{\infty} \frac{(-1)^m}{\sqrt{(r/\xi)^2 + m^2}}, \quad (9)$$

where $U_\xi = e^2/(\varepsilon\xi)$, $\xi \sim 10\text{ nm}$ is the distance between the plates of the metallic contacts and ε is the background dielectric constant. $U_\xi = 25\text{ meV}$ for $\varepsilon = 6$ [5]. For $r > \xi$, the above equation can be simplified to [6, 7],

$$U_2(\mathbf{r}) = U_\xi \frac{2\sqrt{2}e^{-\pi r/\xi}}{\sqrt{r/\xi}}. \quad (10)$$

We use Eq. (9) for $r < \xi$ and Eq. (10) otherwise. In the opposite limit $r/\xi \ll 1$, we regularize the on site Coulomb interaction using a screened potential of the form [8]

$$U_3(\mathbf{r}) = \frac{e^2}{\varepsilon(0.116 + r)} eV = \frac{1.438\text{ eV nm}}{\varepsilon(0.116 + d)nm}. \quad (11)$$

We choose a smooth function that numerically interpolates between (9) and the on-site Hubbard term in (11) as follows

$$U(\mathbf{r}) = \begin{cases} \min(U_1(\mathbf{r}), U_3(\mathbf{r})), & \text{if } r < \xi \\ U_2(\mathbf{r}), & \text{otherwise.} \end{cases} \quad (12)$$

HARTREE-FOCK CALCULATION

Self-consistent loop

The full Hamiltonian is given by the sum of non-interacting and interacting terms as

$$\begin{aligned}
 \mathcal{H} &= \mathcal{H}_0 + \mathcal{H}_I \\
 &= \sum_{\mathbf{k}, \sigma} [\mathcal{H}_0(\mathbf{k}, \sigma) + \mathcal{H}^F(\mathbf{k}, \sigma) + \mathcal{H}^H(\sigma)] \\
 &= \sum_{\mathbf{k}, \sigma} \mathcal{H}(\mathbf{k}, \sigma),
 \end{aligned} \tag{13}$$

where $\mathcal{H}^H(\sigma)$ and $\mathcal{H}^F(\mathbf{k}, \sigma)$ are the Hartree and Fock contributions respectively. In unrestricted Hartree-Fock calculations, crystal momentum \mathbf{k} and spin σ are good quantum numbers. Therefore, the Hamiltonian matrix is block diagonal in the \mathbf{k} and σ spaces. The Hamiltonian matrix corresponding to a moire unit cell with N_b sites has the form

$$\mathcal{H}(\mathbf{k}, \sigma) = \begin{matrix} & \begin{matrix} \beta_1 & \cdots & \beta_{N_b} \end{matrix} \\ \begin{matrix} \alpha_1 \\ \vdots \\ \alpha_{N_b} \end{matrix} & \begin{pmatrix} h_{11}(\mathbf{k}, \sigma) & \cdots & h_{1N_b}(\mathbf{k}, \sigma) \\ \vdots & \ddots & \vdots \\ h_{N_b1}(\mathbf{k}, \sigma) & \cdots & h_{N_bN_b}(\mathbf{k}, \sigma) \end{pmatrix}_{N_b \times N_b} \end{matrix} . \tag{14}$$

We use a Monkhorst-Pack type $N_u = N_1 \times N_2$ grid sampling of \mathbf{k} momentum vectors in the rhombic Brillouin-zone [9]. The sampling of \mathbf{k} vectors is restricted to certain discrete values as follows,

$$\mathbf{k}_{m_1, m_2} = \frac{2m_1 - N_1 - 1}{2N_1} \mathbf{b}_1 + \frac{2m_2 - N_2 - 1}{2N_2} \mathbf{b}_2, \tag{15}$$

where $m_i \in \{1, 2, \dots, N_i\}$ ($i = 1, 2$). \mathbf{b}_1 and \mathbf{b}_2 are moiré lattice vectors in the reciprocal space. We use a grid size $N_1 = N_2 = 9$ with an odd number of k points, such that the Γ and K points are included in the k -mesh. In this prescription, the k -mesh preserves the hexagonal symmetry of the lattice.

We diagonalize each block matrix $\mathcal{H}(\mathbf{k}, \sigma)$ individually and get N_b eigenvalues and corresponding eigenvectors for each \mathbf{k} . Diagonalization of $\mathcal{H}(\mathbf{k}, \sigma)$ gives N_b eigenvalues $E_n(\mathbf{k}, \sigma)$. The n -th column of the matrix

$$\Phi(\mathbf{k}, \sigma) = \begin{matrix} & \begin{matrix} n_1 & \cdots & n_{N_b} \end{matrix} \\ \begin{matrix} \alpha_1 \\ \vdots \\ \alpha_{N_b} \end{matrix} & \begin{pmatrix} \phi_1^1(\mathbf{k}, \sigma) & \cdots & \phi_1^{N_b}(\mathbf{k}, \sigma) \\ \vdots & \ddots & \vdots \\ \phi_{N_b}^1(\mathbf{k}, \sigma) & \cdots & \phi_{N_b}^{N_b}(\mathbf{k}, \sigma) \end{pmatrix}_{N_b \times N_b} \end{matrix} \tag{16}$$

gives the corresponding eigenvector of the n -th band, with $n \in \{1, 2, \dots, N_b\}$. The normalized eigenvectors $\phi_\alpha^n(\mathbf{k}, \sigma)$ form a complete basis and satisfy

$$\sum_{\alpha} \phi_\alpha^{n*}(\mathbf{k}, \sigma) \phi_\alpha^{n'}(\mathbf{k}, \sigma') = \delta_{nn'} \delta_{\sigma\sigma'}, \tag{17}$$

and

$$\sum_n \phi_\alpha^{n*}(\mathbf{k}, \sigma) \phi_\beta^n(\mathbf{k}, \sigma') = \delta_{\alpha\beta} \delta_{\sigma\sigma'}. \tag{18}$$

The number of crystal momenta N_u sampled within the first Brillouin zone is equivalent to the number of unit cells in the real space lattice. The system can accommodate a maximum of N_s spin- σ electrons. In total, there are $N_s = N_u \times N_b$ eigenvalues per spin in a system containing N_s sites in total. We order $2N_s$ states (combining both spin types for all \mathbf{k} vectors) in the ascending order of eigenvalues.

The chemical potential μ is the eigenvalue corresponding to the topmost filled state for a given total number of particles in the system, $N = (N_b + \nu) \times N_u \leq 2N_s$, with N_b the number of sites/atoms per unit cell. In other words, μ is solved self-consistently at a constant electron density ν , which is fixed at each self-consistent iteration by solving

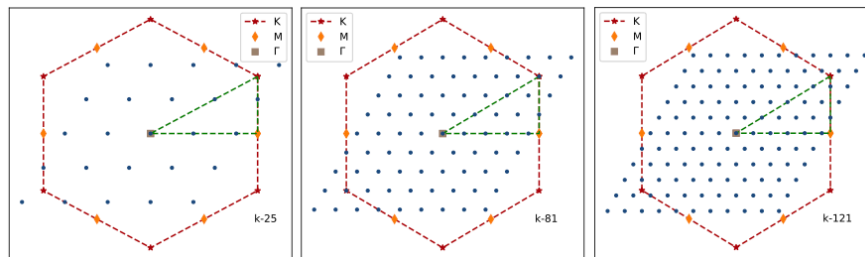


FIG. 2. Coarse graining of momentum in the BZ through a k -mesh with (left to right) 25, 81 and 121 points. Green dashed line: irreducible BZ. All cases include the Γ point. The 9×9 mesh (81 points) we used in the calculation also includes the K points.

the equation

$$\frac{1}{N_u} \sum_{\mathbf{k}, \sigma, n} \theta(\mu - \epsilon_{\mathbf{k}, \sigma, n}) = N_a + \nu. \quad (19)$$

Once we get chemical potential μ , the density matrix in Eq. (29) is calculated by summing over all the occupied states. Hence, the density matrix $\rho(\mathbf{R}, \sigma)$ is the only mean-field parameter in the self-consistent Hartree-Fock calculation. We implement the strong convergence criteria for the density matrix where the root mean square of the difference in density matrices with the previous iteration is less than the tolerance, *i.e.* $(\rho(0, \sigma)_{\text{curr}} - \rho(0, \sigma)_{\text{prev}}) < 10^{-8}$. We use linear mixing for the density matrix,

$$\rho(\mathbf{R}, \sigma)_{\text{prev}} = X \rho(\mathbf{R}, \sigma)_{\text{curr}} + (1 - X) \rho(\mathbf{R}, \sigma)_{\text{prev}}, \quad (20)$$

with mixing coefficient $X = 0.75$. We use this density matrix to build the Hartree and Fock matrices for the next iteration.

Convergence test

The momenta in the BZ is coarse grained over a k -mesh. In order to verify convergence and stability of the calculated self-consistent density matrix with the number of points of the k -mesh, we tested the method considering three different meshes with 25, 81 and 121 points. All tested meshes included the Γ point, whereas the 9×9 mesh (81 points) also included the K points, as shown in Fig. 2. In all meshes we tested, we did not observe any differences in the many-body gaps or in the measurements for SP and QAH states.

The measurements of VP, SLP and AF involve differences of density matrix measurements between different sublattices and are more sensitive to the coarse graining and numerical noise. We observed small differences in the measurements of SLP, VP and AF with different meshes and seeds of random noise in the initial density matrix. The 9×9 mesh was found to be numerically stable in all measurements for different seeds we tested. We did not observe significant numerical improvements in the denser mesh with 121 points compared to the one with 81 points, which was used in all numerical calculations shown in the main text.

Interaction matrix

We consider a four-fermion interaction term for the Coulomb interaction, has no explicit spin dependence:

$$\mathcal{H}_I = \frac{1}{2} \sum_{\alpha\beta} \sum_{ij} \sum_{\sigma\sigma'} U_{\alpha\beta}(\mathbf{R}_j - \mathbf{R}_i) d_{\alpha,i,\sigma}^\dagger d_{\beta,j,\sigma'}^\dagger d_{\beta,j,\sigma'} d_{\alpha,i,\sigma}, \quad (21)$$

where

$$U_{\alpha\beta}(\mathbf{R}_j - \mathbf{R}_i) \equiv U(\mathbf{R}_j + \boldsymbol{\tau}_\beta - \mathbf{R}_i - \boldsymbol{\tau}_\alpha), \quad (22)$$

with τ_α the position of lattice site α with respect to the center of the unit cell located at position \mathbf{R}_i . The Fourier transform of (21) is

$$V = \frac{1}{2} \sum_{\sigma\sigma'} \sum_{\mathbf{k}, \mathbf{k}'} \sum_{\alpha\beta} U_{\alpha\beta}(\mathbf{q}) d_{\mathbf{k}, \alpha, \sigma}^\dagger d_{\mathbf{k}', \beta, \sigma'}^\dagger d_{\mathbf{k}' - \mathbf{q}, \beta, \sigma'} d_{\mathbf{k} + \mathbf{q}, \alpha, \sigma}, \quad (23)$$

with

$$\begin{aligned} U_{\alpha\beta}(\mathbf{q}) &= \frac{1}{N_u} \sum_{\mathbf{R}} U(|\mathbf{R} + \tau_\beta - \tau_\alpha|) e^{i\mathbf{q} \cdot \mathbf{R}} \\ &= \frac{1}{N_u} \sum_{\mathbf{R}} U_{\alpha\beta}(\mathbf{R}) e^{i\mathbf{q} \cdot \mathbf{R}} \end{aligned} \quad (24)$$

the Fourier transform of the Coulomb interaction. The Bravais superlattice vectors $\mathbf{R} = \mathbf{R}_j - \mathbf{R}_i$ are calculated using real space lattice vectors \mathbf{a}_1 and \mathbf{a}_2 as follows

$$R_{m_1, m_2} = m_1 \mathbf{a}_1 + m_2 \mathbf{a}_2, \quad m_i \in \{-L/2, \dots, 0, \dots, L/2\} \quad (25)$$

and the Coulomb interaction is calculated using a list $\mathbf{R}_i = \{R_{m_1, m_2}\}$ of Bravais lattice sites.

The interaction satisfies $U_{\alpha\beta}(\mathbf{R}) = U_{\beta\alpha}(-\mathbf{R})$, and $\hat{U}(\mathbf{R}) = \hat{U}^T(-\mathbf{R})$, and hence $U_{\alpha\beta}(\mathbf{R})$ is not a Hermitian matrix. On the other hand, its Fourier transform $U_{\alpha\beta}(\mathbf{q})$ is Hermitian,

$$U_{\alpha\beta}^\dagger(\mathbf{q}) = U_{\beta\alpha}(-\mathbf{q}) = \frac{1}{N_u} \sum_{\mathbf{R}} U_{\beta\alpha}(\mathbf{R}) e^{-i\mathbf{q} \cdot \mathbf{R}} = \frac{1}{N_u} \sum_{\mathbf{R}} U_{\beta\alpha}(-\mathbf{R}) e^{i\mathbf{q} \cdot \mathbf{R}} = \frac{1}{N_u} \sum_{\mathbf{R}} U_{\alpha\beta}(\mathbf{R}) e^{i\mathbf{q} \cdot \mathbf{R}} = U_{\alpha\beta}(\mathbf{q}). \quad (26)$$

Besides, $\bar{U}_{\alpha\beta}^*(\mathbf{q}) = \bar{U}_{\alpha\beta}(-\mathbf{q})$, since $U_{\alpha\beta}(\mathbf{R})$ is real.

Mean-field decomposition

The expectation value of d -fermions in the Hartree-Fock mean-field basis can be written as

$$\begin{aligned} \langle d_{\mathbf{k}\sigma, \alpha}^\dagger d_{\mathbf{k}'\sigma', \beta} \rangle &\equiv \langle \text{MF} | d_{\mathbf{k}\sigma, \alpha}^\dagger d_{\mathbf{k}'\sigma', \beta} | \text{MF} \rangle \\ &= \sum_n \phi_\alpha^{n*}(\mathbf{k}, \sigma) \phi_\beta^n(\mathbf{k}', \sigma') \theta(\mu - \epsilon_{\mathbf{k}, n}) \delta_{\mathbf{k}\mathbf{k}'} \delta_{\sigma\sigma'} \\ &= \sum_n^{\text{occ}} \phi_\alpha^{n*}(\mathbf{k}, \sigma) \phi_\beta^n(\mathbf{k}', \sigma') \delta_{\mathbf{k}\mathbf{k}'} \delta_{\sigma\sigma'}, \end{aligned} \quad (27)$$

summed over all the occupied bands. From Eq. (27), the momentum space density matrix can be written as

$$\begin{aligned} \bar{\rho}_{\alpha\beta}(\mathbf{k}, \sigma) &= \langle \text{MF} | d_{\mathbf{k}\sigma, \beta}^\dagger d_{\mathbf{k}\sigma, \alpha} | \text{MF} \rangle \\ &= \sum_n^{\text{occ}} \phi_\beta^{n*}(\mathbf{k}, \sigma) \phi_\alpha^n(\mathbf{k}, \sigma). \end{aligned} \quad (28)$$

Here, $\bar{\rho}(\mathbf{k}, \sigma) = \bar{\rho}^*(-\mathbf{k}, \sigma)$. The real-space density matrix is defined as

$$\begin{aligned} \rho_{\alpha\beta}(\mathbf{R}, \sigma) &= \frac{1}{N_u} \sum_{\mathbf{k}} \sum_n^{\text{occ}} e^{-i\mathbf{k} \cdot \mathbf{R}} \phi_\beta^{n*}(\mathbf{k}, \sigma) \phi_\alpha^n(\mathbf{k}, \sigma) \\ &= \frac{1}{N_u} \sum_{\mathbf{k}} e^{-i\mathbf{k} \cdot \mathbf{R}} \bar{\rho}_{\alpha\beta}(\mathbf{k}, \sigma) \end{aligned} \quad (29)$$

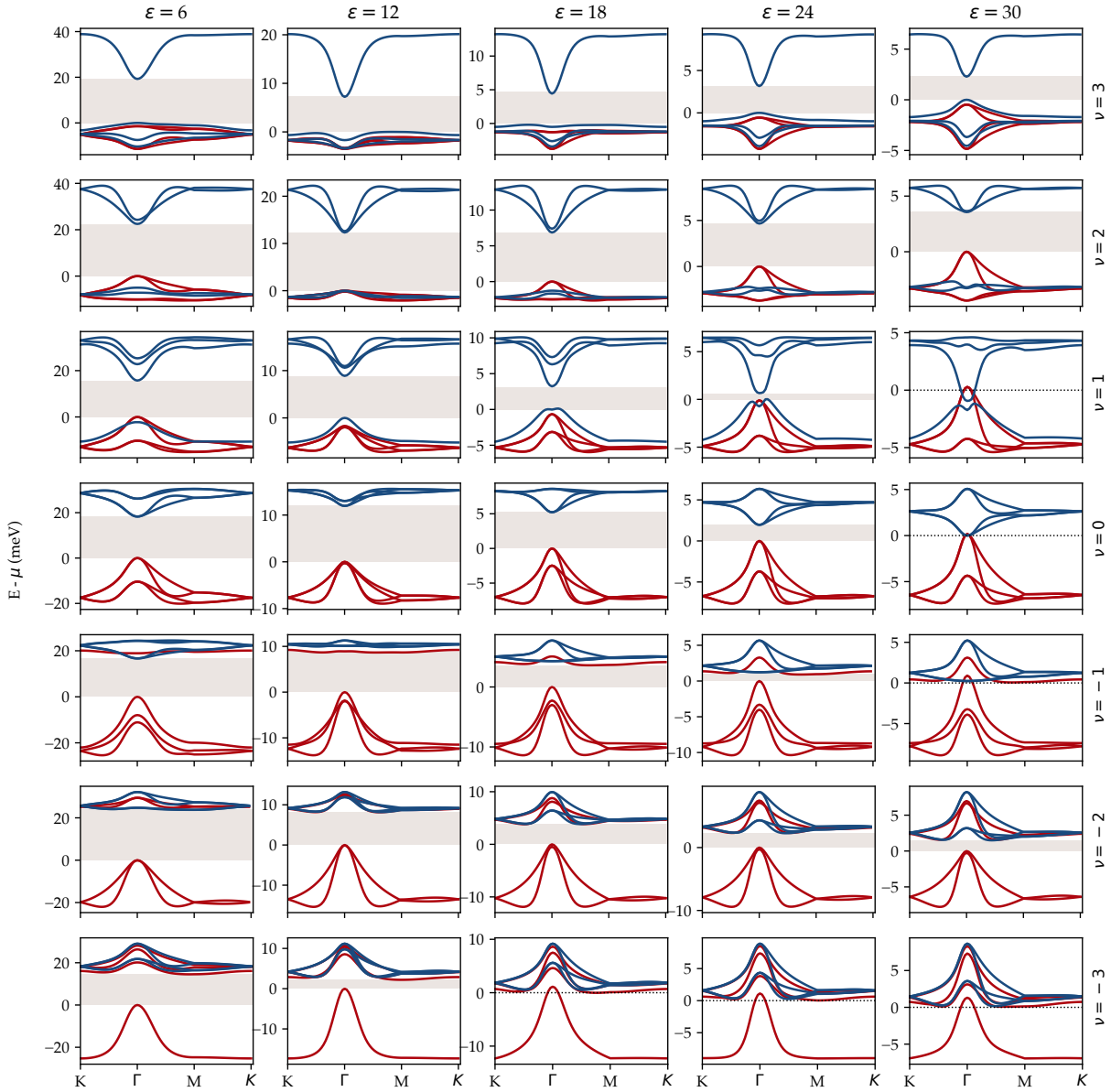


FIG. 3. Band structure of the low energy bands for dielectric constants $\varepsilon = 6, 12, 18, 24$ and 30 at integer filling factors, from $\nu = 3$ to $\nu = -3$ (top to bottom). Red lines: spin σ ; blue lines: spin $-\sigma$. The gray region indicates the many-body transport gap. All bands in red (blue) are topological for $\nu < 0$ ($\nu > 0$) and trivial otherwise. The Chern numbers of all occupied bands add up to 1 at odd fillings and to 0 at even fillings. Energies measured away from the chemical potential μ .

where the diagonal element $\rho_\alpha(0, \sigma)$ is the average particle density of spin σ at site α . The trace $\text{Tr}(\rho_{\alpha\beta}(0, \sigma))$ gives the average number of spin σ particles per unit cell. From the general properties of the density matrix [10],

$$\bar{\rho}_{\alpha\beta}(\mathbf{k}, \sigma) = \bar{\rho}_{\beta\alpha}^*(\mathbf{k}, \sigma) = \bar{\rho}_{\beta\alpha}(-\mathbf{k}, \sigma) = \bar{\rho}_{\alpha\beta}^*(-\mathbf{k}, \sigma), \quad (30)$$

and

$$\rho_{\alpha\beta}(\mathbf{R}, \sigma) = \rho_{\beta\alpha}^\dagger(-\mathbf{R}, \sigma), \quad (31)$$

then $\rho(\mathbf{R}, \sigma) = \rho^\dagger(-\mathbf{R}, \sigma)$. I.e., $\rho(0, \sigma)$ is an Hermitian matrix. The density matrix $\rho_{\alpha\beta}(\mathbf{R}, \sigma)$ is used as a self-consistency parameter in the numerical calculation. It is diagonal if all the states are fully occupied with $N = 2 * N_s$ (or $\nu = N_b$).

In the mean-field decomposition, Coulomb interaction in Eq. (23) can be separated into direct (Hartree) and exchange (Fock) terms,

$$\begin{aligned}
\mathcal{H}_I^H &\approx \frac{1}{2} \sum_{\sigma\sigma'} \sum_{\mathbf{k}, \mathbf{k}', \mathbf{q}} \sum_{\alpha\beta} \left[\bar{U}_{\alpha\beta}(\mathbf{q}) d_{\mathbf{k}\sigma, \alpha}^\dagger d_{\mathbf{k}+\mathbf{q}\sigma, \alpha} \langle d_{\mathbf{k}'\sigma', \beta}^\dagger d_{\mathbf{k}'+\mathbf{q}\sigma', \beta} \rangle + \bar{U}_{\alpha\beta}(\mathbf{q}) \langle d_{\mathbf{k}\sigma, \alpha}^\dagger d_{\mathbf{k}+\mathbf{q}\sigma, \alpha} \rangle d_{\mathbf{k}'\sigma', \beta}^\dagger d_{\mathbf{k}'-\mathbf{q}\sigma', \beta} \right] \\
&= \sum_{\sigma, \sigma'} \sum_{\mathbf{k}, \mathbf{k}'} \sum_{\alpha\beta} \sum_n^{\text{occ}} \bar{U}_{\alpha\beta}(0) \phi_\beta^{n*}(\mathbf{k}', \sigma') \phi_\beta^n(\mathbf{k}', \sigma) d_{\mathbf{k}\sigma, \alpha}^\dagger d_{\mathbf{k}\sigma, \alpha} \\
&= \sum_{\sigma, \sigma'} \sum_{\mathbf{k}, \mathbf{k}'} \sum_{\alpha\beta} \sum_n^{\text{occ}} \frac{1}{N_u} \sum_{\mathbf{R}} U_{\alpha\beta}(\mathbf{R}) \phi_\beta^{n*}(\mathbf{k}', \sigma') \phi_\beta^n(\mathbf{k}', \sigma) d_{\mathbf{k}\sigma, \alpha}^\dagger d_{\mathbf{k}\sigma, \alpha} \\
&= \sum_{\sigma, \mathbf{k}, \alpha} h_\alpha^H(\sigma) d_{\mathbf{k}\sigma, \alpha}^\dagger d_{\mathbf{k}\sigma, \alpha}
\end{aligned} \tag{32}$$

and

$$\begin{aligned}
\mathcal{H}_I^F &\approx -\frac{1}{2} \sum_{\sigma\sigma'} \sum_{\mathbf{k}, \mathbf{k}', \mathbf{q}} \sum_{\alpha\beta} \left[\bar{U}_{\alpha\beta}(\mathbf{q}) d_{\mathbf{k}\sigma, \alpha}^\dagger d_{\mathbf{k}'-\mathbf{q}\sigma', \beta} \langle d_{\mathbf{k}'\sigma', \beta}^\dagger d_{\mathbf{k}+\mathbf{q}\sigma, \alpha} \rangle + \bar{U}_{\alpha\beta}(\mathbf{q}) \langle d_{\mathbf{k}\sigma, \alpha}^\dagger d_{\mathbf{k}'-\mathbf{q}\sigma', \beta} \rangle d_{\mathbf{k}'\sigma', \beta}^\dagger d_{\mathbf{k}+\mathbf{q}\sigma, \alpha} \right] \\
&= -\sum_{\sigma} \sum_{\mathbf{k}} \sum_{\alpha\beta} \sum_{\mathbf{k}'} \sum_n^{\text{occ}} \bar{U}_{\alpha\beta}(\mathbf{k}' - \mathbf{k}) \phi_\beta^{n*}(\mathbf{k}', \sigma) \phi_\alpha^n(\mathbf{k}', \sigma) d_{\mathbf{k}\sigma, \alpha}^\dagger d_{\mathbf{k}\sigma, \beta} \\
&= -\sum_{\sigma} \sum_{\mathbf{k}} \sum_{\alpha\beta} \sum_{\mathbf{k}'} \sum_n^{\text{occ}} \frac{1}{N_u} \sum_{\mathbf{R}} e^{-i(\mathbf{k}' - \mathbf{k}) \cdot \mathbf{R}} U_{\alpha\beta}(\mathbf{R}) \phi_\beta^{n*}(\mathbf{k}', \sigma) \phi_\alpha^n(\mathbf{k}', \sigma) d_{\mathbf{k}\sigma, \alpha}^\dagger d_{\mathbf{k}\sigma, \beta} \\
&= -\sum_{\sigma, \mathbf{k}} \sum_{\alpha\beta} h_{\alpha\beta}^F(\mathbf{k}, \sigma) d_{\mathbf{k}\sigma, \alpha}^\dagger d_{\mathbf{k}\sigma, \beta}
\end{aligned} \tag{33}$$

where

$$h_\alpha^H(\sigma) = \sum_{\beta, \sigma'} \sum_{\mathbf{R}} U_{\alpha\beta}(\mathbf{R}) \rho_\beta(0, \sigma'), \tag{34}$$

and

$$h_{\alpha\beta}^F(\mathbf{k}, \sigma) = \sum_{\mathbf{R}} e^{i\mathbf{k} \cdot \mathbf{R}} U_{\alpha\beta}(\mathbf{R}) \rho_{\alpha\beta}(\mathbf{R}, \sigma) \tag{35}$$

are the Hartree and Fock matrix elements, respectively. All densities are measured away from the neutrality point. We subtract a uniform background of charge from the density matrix, $\rho_{\alpha, \beta}(\mathbf{R}, \sigma) \rightarrow \rho_{\alpha, \beta}(\mathbf{R}, \sigma) - \frac{1}{2} \delta_{\alpha, \beta} \delta_{\mathbf{R}, 0}$.

Once the real space density matrix is found to converge, the band structure of the many-body problem is extracted from the diagonalization of the Hartree-Fock Hamiltonian and calculated over a k -path passing through high symmetry points. The band structure of the low energy bands for $\varepsilon = 6, 12, 18, 24$ and 30 are shown in Fig. 3 of the SM for integer filling factors $\nu \in [-3, 3]$.

Numerical measurements

We performed numerical measurements using the density matrix, as described in the main text. In table I we report the contribution from both the low energy flat bands (FB) and remote bands (RB) to the different order parameters for $\varepsilon = 6, 12, 18, 24$ and 30 . We find that the spin polarization (SP) describes a ferromagnetic state that is restricted to the flat bands, with the remote bands having zero net polarization. Antiferromagnetism (AF) and sublattice polarization (SLP) measurements in the low energy flat bands are correlated (see table I), indicating the presence of spin modulation in the flat bands with the period of a lattice constant. With the exception of $\nu = 0$ and -2 , we observe that all other integer fillings are sublattice polarized. SLP also correlates with the emergence of a staggered AF order in the remote bands.

The pattern of charge distribution and spin polarization of the flat bands in the moire unit cell are shown in Fig.

Order parameters for $\varepsilon = 6$

OP \ ν	-3		-2		-1		0		1		2		3	
	RB	FB												
SP	0.00	1.00	0.00	2.00	0.00	3.00	0.00	4.00	0.00	3.00	0.00	2.00	0.00	1.00
AF	0.16	0.12	0.00	0.00	0.20	0.15	0.00	0.00	0.26	0.20	0.06	0.04	0.20	0.16
SLP	0.08	0.12	0.00	0.00	0.10	0.15	0.00	0.00	0.12	0.20	0.03	0.04	0.10	0.16
QAH	0.17	0.22	0.00	0.00	0.17	0.23	0.00	0.00	0.16	0.23	0.00	0.00	0.16	0.23
VP	0.00	0.13	0.00	0.01	0.00	0.15	0.00	0.00	0.00	0.20	0.00	0.22	0.00	0.16

Order parameters for $\varepsilon = 12$

OP \ ν	-3		-2		-1		0		1		2		3	
	RB	FB												
SP	0.00	1.00	0.00	2.00	0.00	3.00	0.00	4.00	0.00	3.00	0.00	2.00	0.00	1.00
AF	0.07	0.12	0.00	0.00	0.11	0.20	0.00	0.00	0.09	0.16	0.01	0.02	0.07	0.14
SLP	0.04	0.12	0.00	0.00	0.07	0.20	0.00	0.00	0.05	0.16	0.01	0.02	0.04	0.14
QAH	0.07	0.18	0.00	0.00	0.07	0.19	0.00	0.00	0.07	0.19	0.00	0.00	0.07	0.19
VP	0.00	0.14	0.00	0.28	0.00	0.23	0.00	0.00	0.00	0.18	0.00	0.32	0.00	0.16

Order parameters for $\varepsilon = 18$

OP \ ν	-3		-2		-1		0		1		2		3	
	RB	FB												
SP	0.00	1.00	0.00	2.00	0.00	3.00	0.00	4.00	0.00	3.00	0.00	2.00	0.00	1.00
AF	0.03	0.08	0.00	0.00	0.05	0.14	0.00	0.00	0.03	0.09	0.01	0.02	0.05	0.13
SLP	0.02	0.08	0.00	0.00	0.03	0.14	0.00	0.00	0.02	0.09	0.01	0.02	0.03	0.13
QAH	0.03	0.12	0.00	0.00	0.04	0.17	0.00	0.00	0.03	0.11	0.00	0.00	0.04	0.17
VP	0.00	0.15	0.00	0.20	0.00	0.18	0.00	0.00	0.00	0.18	0.00	0.16	0.00	0.18

Order parameters for $\varepsilon = 24$

OP \ ν	-3		-2		-1		0		1		2		3	
	RB	FB												
SP	0.00	1.00	0.00	2.00	0.00	3.00	0.00	4.00	0.00	3.00	0.00	2.00	0.00	1.00
AF	0.03	0.12	0.00	0.00	0.02	0.09	0.00	0.00	0.01	0.04	0.01	0.02	0.03	0.12
SLP	0.02	0.12	0.00	0.00	0.01	0.09	0.00	0.00	0.01	0.04	0.01	0.02	0.02	0.12
QAH	0.03	0.15	0.00	0.00	0.03	0.16	0.00	0.00	0.01	0.05	0.00	0.00	0.03	0.15
VP	0.00	0.18	0.00	0.09	0.00	0.12	0.00	0.00	0.00	0.19	0.00	0.08	0.00	0.19

Order parameters for $\varepsilon = 30$

OP \ ν	-3		-2		-1		0		1		2		3	
	RB	FB												
SP	0.00	1.00	0.00	2.00	0.00	3.00	0.00	3.95	0.00	2.95	0.00	2.00	0.00	1.00
AF	0.02	0.11	0.00	0.00	0.02	0.07	0.00	0.00	0.00	0.02	0.01	0.02	0.02	0.09
SLP	0.02	0.11	0.00	0.00	0.01	0.07	0.00	0.00	0.00	0.02	0.01	0.02	0.01	0.09
QAH	0.02	0.13	0.00	0.00	0.02	0.14	0.00	0.00	0.00	0.03	0.00	0.00	0.02	0.14
VP	0.00	0.18	0.00	0.04	0.00	0.11	0.00	0.00	0.00	0.14	0.00	0.02	0.00	0.17

TABLE I. Contributions from the flat bands (FB) and remote bands (RB) to the order parameters. SP: spin polarization; AF: antiferromagnetism. SLP: sublattice polarization; QAH: quantum anomalous Hall; VP: valley polarization.

4. The charge distribution shown in panel 4a accumulates at the corners of the unit cell, near the AA site regions. This region (orange diamond) is shown in detail in panel 4b. The spin polarization pattern is shown in Fig. 4c. The red diamond on the corner is shown in detail in panel 4d. The spin polarization has a sublattice modulation that becomes more pronounced near AA sites. This pattern of polarization is absent at half and quarter filling ($\nu = 0$ and $\nu = -2$), but was observed in the insulating phases at all other integer fillings.

Our measurements of loop currents on the lattice indicates the emergence of a quantum anomalous Hall (QAH) state at odd filling factors. Interestingly, we find contributions to QAH order parameter not only in the flat bands, but also in some of the remote bands, which can be topological. At even filling factors we measured zero net contribution to the QAH order parameter both in the flat bands as in the remote ones. The detailed results of the measurements can be found on table I.

We note that at $\nu = -3$ the system undergoes a MIT below $\varepsilon = 18$, where the many-body transport gap closes, even though a finite optical gap is still present at all momenta in the BZ. The band structure shown in Fig. 3 (bottom panel on the right) indicates that this state describes a spin polarized metal with a finite Fermi surface around the Γ

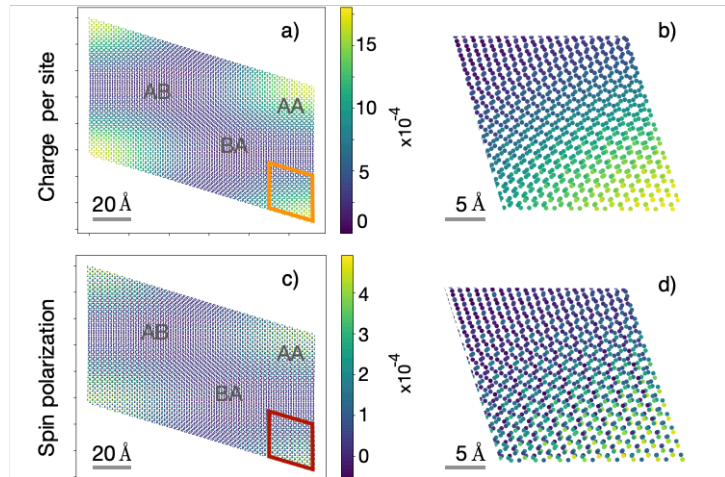


FIG. 4. Charge and spin distribution on the Moiré unit cell in magic angle TBG for $\varepsilon = 6$ and $\nu = 3$. a) Charge per site $\hat{\rho}_{\alpha\alpha}(0, \sigma)$ of the low energy flat bands, concentrated near AA regions, at the corners on the unit cell (orange diamond), shown in b). The zoomed charge pattern shows sublattice symmetry breaking (SLP order). c) Spin polarization favors ferromagnetism, with amplitude modulation at the sublattice scale near AA sites (red diamond), as shown in d).

point. The measurements of the QAH order parameter are non-zero, revealing loop currents in the bulk. While the corresponding edge states are in principle allowed to form inside the optical gap, they do not translate in topologically protected chiral edge states immune to backscattering effects, since the system has a Fermi surface. In that sense, a Chern number is not well defined. The same applies to the metallic states at $\nu = \pm 1$ for $\varepsilon = 30$, which have a finite QAH order parameter, indicating the presence of chiral loop currents in bulk, but no well defined Chern number.

We verified the topological nature of the flat bands by explicitly calculating their Chern number. At negative fillings ($\nu < 0$) the spin σ bands (red lines in Fig. 3) are topological whereas the spin $-\sigma$ ones (blue) are topologically trivial. This pattern reverses at positive fillings ($\nu > 0$), with the spin σ bands becoming trivial and the spin $-\sigma$ bands (blue) topological. We numerically observe that inversion symmetry is broken between the eigenvalues $E(\mathbf{k})$ and $E(-\mathbf{k})$ of all topological flat bands, but is preserved in the topologically trivial ones. At the neutrality point ($\nu = 0$) all the bands are trivial. In all insulating states the Chern numbers of the occupied flat bands add up to 1 for odd filling factors and zero otherwise.

We also checked the nature of the ground state at non-integer filling factors according to the unrestricted HF calculation. In Fig. 5 we plot the band structure for $\varepsilon = 6$ and $\nu = 0.5$. The Fermi surface has two sheets, both with the same spin ($-\sigma$). In all cases, we find that the chemical potential crosses the low energy bands and gives rise to a spin polarized metal.

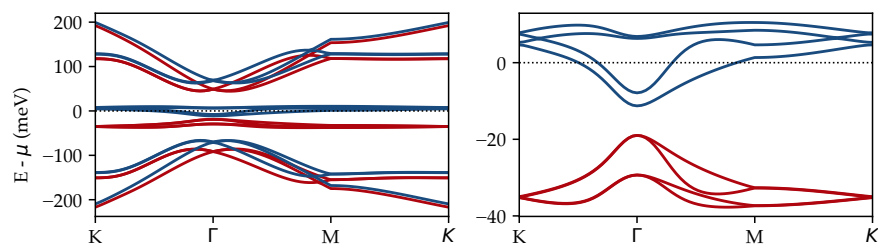


FIG. 5. Band structure of the low energy bands at $\nu = 0.5$ for $\varepsilon = 6$ showing some of the remote bands. Red lines: spin σ ; Blue lines: spin $-\sigma$. On the right, we zoom in around the low energy flat bands. The chemical potential μ crosses the spin $-\sigma$ bands (blue lines) above the many-body gap. The ground state is described by a spin polarized metal.

* Electronic address: khagendra.adhikari@ou.edu

† Electronic address: uchoa@ou.edu

- [1] P. Moon and M. Koshino, Optical absorption in twisted bilayer graphene, *Phys. Rev. B* **87**, 205404 (2013).
- [2] J. C. Slater and G. F. Koster, Simplified lcao method for the periodic potential problem, *Phys. Rev.* **94**, 1498 (1954).
- [3] M. Koshino, N. F. Q. Yuan, T. Koretsune, M. Ochi, K. Kuroki, and L. Fu, Maximally localized wannier orbitals and the extended hubbard model for twisted bilayer graphene, *Phys. Rev. X* **8**, 031087 (2018).
- [4] K. Uchida, S. Furuya, J.-I. Iwata, and A. Oshiyama, Atomic corrugation and electron localization due to moiré patterns in twisted bilayer graphenes, *Phys. Rev. B* **90**, 155451 (2014).
- [5] B. A. Bernevig, Z.-D. Song, N. Regnault, and B. Lian, Twisted bilayer graphene. iii. interacting hamiltonian and exact symmetries, *Phys. Rev. B* **103**, 205413 (2021).
- [6] J. González and T. Stauber, Magnetic phases from competing hubbard and extended coulomb interactions in twisted bilayer graphene, *Phys. Rev. B* **104**, 115110 (2021).
- [7] R. E. Throckmorton and O. Vafek, Fermions on bilayer graphene: Symmetry breaking for $b = 0$ and $\nu = 0$, *Phys. Rev. B* **86**, 115447 (2012).
- [8] L. Rademaker, D. A. Abanin, and P. Mellado, Charge smoothening and band flattening due to hartree corrections in twisted bilayer graphene, *Phys. Rev. B* **100**, 205114 (2019).
- [9] H. J. Monkhorst and J. D. Pack, Special points for brillouin-zone integrations, *Phys. Rev. B* **13**, 5188 (1976).
- [10] R. A. Evarestov, *Quantum Chemistry of Solids* (Springer Berlin Heidelberg, 2012).